Some Three-Dimensional Characteristics of Low-Frequency Current Fluctuations near the Oregon Coast

PIJUSH K. KUNDU AND J. S. ALLEN

School of Oceanography, Oregon State University, Corvallis 97331

(Manuscript received 25 April 1975, in revised form 18 August 1975)

ABSTRACT

An analysis is presented of the low-frequency fluctuations $[\omega < 0.6$ cycle per day (cpd)$]$ of the currents near the Oregon coast, based on the 1972 and 1973 measurements from moored current meters in CUE-1 and CUE-2. Let u and v denote the eastward (approximately onshore) and northward (approximately alongshore) components of the currents. The mean alongshore velocity $\bar{v}$ has the structure of a baroclinic coastal jet, whose maximum speed occurs near the surface at a distance of about 15–20 km from the shore, whereas the fluctuating part of v has the structure of a roughly barotropic coastal jet whose maximum occurs very near (<4 km) the shore. The standard deviation of v is approximately depth-independent whereas that of u decreases with depth. As one approaches the coast, the standard deviation of u decreases whereas that of v rises steeply, consistent with the behavior expected of coastally trapped wave motion. A scatter plot of the velocity fluctuations in a hodograph plane indicates that the fluctuations roughly follow the direction of the local isobaths. The Reynolds stresses in an east-north coordinate system therefore change sign because of the change of direction of the isobaths in the region. The v fluctuations seem to be mutually better correlated than the u fluctuations throughout the region, suggesting that the u components may be affected by "turbulence." By finding the time lag corresponding to maximum correlation between stations separated alongshore, the velocity fluctuations have been found to propagate northward approximately nondispersively at a mean velocity of about 500 km day^{-1} during 1972 and 120 km day^{-1} during 1973. A method for performing the empirical orthogonal decomposition for two-dimensional vector time series has been formulated and applied to the velocity field over the continental shelf.

1. Introduction

The phenomenon of coastal upwelling off the Oregon coast in the summer months due to a predominantly southward wind has been studied extensively in recent years (Smith, 1974; Kundu *et al.*, 1975; Halpern, 1975). There have been two Coastal Upwelling Experiments off the Oregon coast, CUE-1 during the summer of 1972 and CUE-2 during the summer of 1973. Based on the 1972 measurements at one station (DB7), Smith (1974) noted the dominance of depth-independent current fluctuations, the strong correlation of the sea level depression at the coast with the southward current fluctuations, and the correlation of the north-south components of the wind and the current fluctuations. Based on the DB7 observations of 1972 and those of the station *Carnation* in 1973, Kundu *et al.* (1975) performed a modal decomposition to formally separate the barotropic and baroclinic components. They found a correlation of the baroclinic component of the current fluctuation at DB7 and the temperature fluctuation at a depth of 40 m at the same station. Halpern (1975) concentrated on the structure of. a coastal upwelling event and, based on measurements at *Carnation*, including those from several current meters near the surface, concluded that during the event the onshore and offshore transports were approximately balanced.

Utilizing hydrographic observations, he also found an approximate exponential decrease of vertical velocity with offshore distance. All the above work concerning horizontal currents was based primarily on observations at a single station. Huyer *et al.* (1975) have examined the correlation of the current, wind, and the sea level fluctuations off the coast of Oregon and Washington during the upwelling season. They found that during 1972 the north-south fluctuations at a depth of about 60 m off the coasts of Oregon and Washington, separated by an alongshore distance of about 200 km, had a correlation coefficient as high as 0.86.

We have undertaken a study of the three-dimensional characteristics of the upwelling flow field, with an emphasis on the relationship of the current fluctuations at various stations. An analysis of the measurements made during CUE-1 and CUE-2 at all stations and depths will be presented here in order to describe the three-dimensional behavior of the low-frequency $[\omega < 0.6$ cycle per day (cpd)$]$ current fluctuations in the upwelling region.

2. Observations

The locations of the current meters for the CUE-1 and CUE-2 experiments are shown in Fig. 1. The CUE-1 moorings consist of the Newport hydrographic
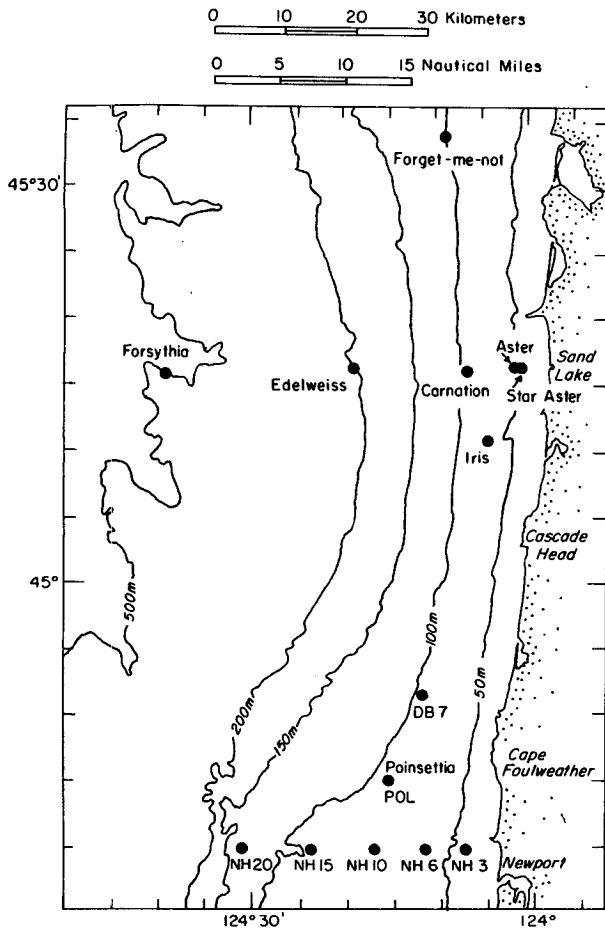
FIG. 1. Locations of current meters during CUE-1 and CUE-2. The CUE-1 array is composed of the NH, POL and DB stations. The CUE-2 is composed of the stations named after flowers. The bathymetric contours are in meters. In 1972, the data from an additional current meter station UWIN in 73 m of water was available. It was located at 46°50′N, 124°50′W, about 200 km N of the NH line (see Fig. 1 of Huyer et al., 1975). The locations of POL during CUE-1 and Poinsettia during CUE-2 were identical.

(NH) stations, the Depoe Bay (DB) stations, and POL, with the number attached therewith denoting the distance from the coast in nautical miles. For example, NH15 is at a distance of 15 n mi from the coast. The CUE-2 moorings are denoted by names of flowers, and are generally placed northward of the CUE-1 array. Currents and temperatures were measured with Aanderaa current meters suspended beneath subsurface floats. In 1972, the wind and atmospheric pressure were measured at Newport, whereas the sea level was measured by a tide gage at Depoe Bay. In 1973, the wind, atmospheric pressure, and sea level were all measured at Newport. The acquisition and processing of the time series data are described by Pillsbury et al. (1974). In addition to the CUE-1 and CUE-2 data, current meter measurements from another station in 73 m of water, called UWIN, located about 200 km northward of the NH line at (46°50′N, 124°50′W), and wind measure-

ments near this station at Westport, Wash., are used. These measurements were taken by the University of Washington and reported by Huyer et al. (1975).

The lengths of the time series for velocity and temperature records at various stations are indicated in Fig. 2. The data processing, described in more detail in Smith (1974) and Kundu et al. (1975), included filtering of the 5–10 min observations to obtain hourly time series, and refiltering these to eliminate the tidal and inertial frequencies by means of a filter having 121 weights with a half-power point of 40 h (0.6 cpd). We shall, therefore, be concerned here with frequencies $\lesssim 0.6$ cpd.

Since there was a gap (4–11 August) in the Poinsettia records, all the calculations involving that station were performed for the two segments separately, and a weighted average of the results was taken.

3. Mean and standard deviation

All quantities will be referred to a Cartesian coordinate system (x,y,z) with x positive eastward, y positive northward, and z positive upward, with the origin placed at the coast. The time mean of a variable will be indicated by an overbar, and its time fluctuation
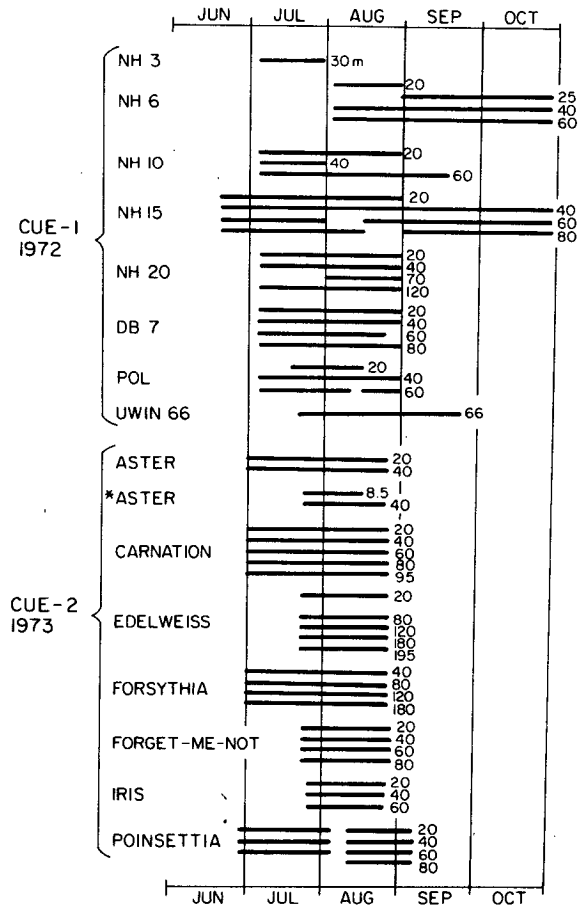

FIG. 2. The lengths of time series at different stations.

TABLE 1. Mean, standard deviation, Reynolds stress and principal axis for CUE-1 stations.

Station	Depth (m)	$\bar{u}$ (cm s⁻¹)	$\bar{v}$ (cm s⁻¹)	u_{SD} (cm s⁻¹)	v_{SD} (cm s⁻¹)	$\overline{u'v'}$ (cm² s⁻²)	$\dfrac{\overline{u'v'}}{u_{SD}v_{SD}}$	Major principal axis[a] (deg)	Mean flow orientation[c] (deg)
NH3	30	-0.2	1.4	2.6	14.3	20.9	0.57	-6	8
NH6	20	-1.7	1.3	6.7	15.5	90.2	0.87	-21	53
	25	-0.6	3.2	6.7	15.6	64.0	0.61	-16	11
	40	0.7	2.8	5.6	13.5	51.6	0.68	-17	-14
	(40)[b]	-1.7	5.3	5.5	12.7	62.4	0.89	-22	18
	60	-0.7	2.2	2.4	9.0	11.6	0.54	-9	18
	(60)	-2.3	2.9	2.5	9.7	19.4	0.80	-12	38
NH10	20	-6.4	-14.3	5.8	10.6	32.7	0.53	-20	156
	40	-3.5	-5.1	6.8	12.8	63.0	0.73	-23	146
	60	-2.7	-0.2	4.9	10.7	41.2	0.79	-21	94
NH15	20	-7.5	-9.0	7.4	9.1	24.3	0.36	-30	140
	40	-2.6	-4.7	6.7	8.8	38.3	0.65	-33	151
	(40)	-2.1	-3.8	6.5	8.2	33.1	0.63	-35	151
	60	0.3	0.3	6.9	8.1	29.3	0.52	-36	-45
	(60)	0.6	0.7	7.9	6.5	29.4	0.57	-54	-41
	80	1.0	3.7	6.1	5.2	13.1	0.41	-56	-15
	(80)	2.3	4.2	7.3	5.6	20.2	0.50	-59	-29
NH20	20	-4.8	-4.6	7.4	7.6	22.0	0.39	-43	134
	40	-3.0	-1.8	6.8	8.9	31.9	0.53	-32	121
	70	1.2	7.3	4.1	7.0	17.4	0.61	-24	-9
	120	0.1	9.0	2.4	9.4	9.2	0.41	-6	-1
DB7	20	-3.4	-18.1	5.2	12.0	22.9	0.37	-10	169
	40	0.4	-7.9	6.0	13.4	33.1	0.46	-14	-177
	60	2.6	1.6	4.9	14.5	50.7	0.71	-14	-58
	80	3.1	6.1	4.1	13.8	42.3	0.75	-13	-27
UWIN	66	-1.5	6.5	2.5	9.0	-12.2	-0.55	9	13
POL	40	0.7	-5.9	6.0	9.8	48.1	0.82	-29	-173

[a] Measured counterclockwise from north. One can, of course, add ±180° to these values.

[b] Parentheses indicate that the months of September and October have been omitted.

[c] Direction *to* which the current flows, measured counterclockwise from north.

will be indicated by a prime. The eastward, northward and upward velocities will be denoted by u, v and w respectively, so that at point $\mathbf{x}$ the eastward velocity is

$$u(\mathbf{x},t) = \bar{u}(\mathbf{x}) + u'(\mathbf{x},t), \quad \bar{u}' = 0. \tag{3.1}$$

The standard deviation of a quantity will be denoted by a suffix SD, so that

$$u_{SD} = [\overline{u'^2}]^{\frac{1}{2}}. \tag{3.2}$$

The means and standard deviations of the eastward and northward components of the currents at various stations are given in Tables 1 and 2 for CUE-1 and CUE-2, respectively.[1] They are computed for the entire lengths of the respective records as shown in Fig. 2. Sometimes these included the months of September and October, which are not considered very typical of the upwelling season off Oregon. In such cases (e.g., the 40 and 60 m currents at NH6) the means and standard deviations are also computed by deleting these two

[1] An earlier version of this paper contained results from the 40 m depth at *Edelweiss*. However, it now appears that the direction sensor of this current meter was probably faulty. We have, therefore, omitted here the results relating to this current meter.

months from the records; the resulting values are recorded in parentheses in these tables.

An examination of the $\bar{u}$ values shows that during the CUE-2 experiment most of the currents below 10 m were eastward, except at stations *Edelweiss* and *Poinsettia*. With some exceptions, the CUE-1 and *Poinsettia* records showed a general trend of eastward velocity below mid-depth and westward velocity above mid-depth.

Fig. 3 shows the variation of $\bar{v}$ at various depths as a function of distance from shore. The mean current seems to be in the form of a baroclinic coastal jet, whose maximum speed occurs near the surface at a distance of about 15–20 km from the shore. There is a vertical shear in the mean velocity, so that the surface layers are moving southward relative to the deeper layers, consistent with the upward-toward-the-coast slope of the mean isopycnals throughout the upwelling season (see, e.g., Fig. 2 of Kundu *et al.*, 1975). Adjacent to the coast the mean flow at all depths seems to be northward for the CUE-1 line. This may be due to the backflow accompanying a separation of the jet at Cape Foulweather. However, the mean values near the coast

TABLE 2. Mean, standard deviation, Reynolds stress and principal axis for CUE-2 stations.

Station	Depth (m)	$\bar{u}$ (cm s⁻¹)	$\bar{v}$ (cm s⁻¹)	u_{SD} (cm s⁻¹)	v_{SD} (cm s⁻¹)	$\overline{u'v'}$ (cm⁻² s⁻²)	$\dfrac{\overline{u'v'}}{u_{SD}v_{SD}}$	Major principal axis[a] (deg)	Mean flow orientation[b] (deg)
*Aster	8	−2.3	−2.6	5.2	16.5	17.8	0.21	−4	139
	40	0.8	−3.6	2.1	13.9	−0.0	−0.00	0	167
Aster	20	6.0	−11.3	4.0	12.5	−1.8	−0.04	1	−152
	40	−0.6	−0.9	1.6	9.4	−4.1	−0.27	3	146
Carnation	20	3.2	−23.9	4.7	10.0	−1.0	−0.02	1	−172
	40	4.3	−10.9	3.0	10.5	−3.6	−0.11	2	−158
	60	2.7	−2.0	2.9	11.7	−1.6	−0.05	1	−127
	80	1.1	2.9	2.0	10.7	−6.8	−0.32	4	−21
	95	0.6	2.5	1.7	8.4	−6.4	−0.46	6	−13
Edelweiss	20	2.4	−21.7	4.3	6.1	−19.5	−0.75	32	−174
	80	2.6	−4.6	2.3	5.5	−5.0	−0.40	11	−151
	120	2.0	2.5	1.9	5.4	−0.7	−0.07	2	−37
	180	−1.8	7.3	1.7	5.4	−5.9	−0.64	12	14
	195	−1.7	5.5	2.4	4.9	−8.7	−0.76	22	17
Iris	20	−0.3	−18.2	2.9	10.4	9.1	0.31	−5	179
	40	1.9	−8.0	2.9	12.2	21.0	0.59	−8	−167
	60	0.2	−0.3	1.9	11.2	14.9	0.71	−7	−146
Forsythia	40	1.1	−12.6	2.4	4.0	−5.2	−0.54	24	−175
	80	0.2	−8.0	1.5	3.5	−1.6	−0.30	9	−179
	120	0.2	−4.3	1.3	3.3	−0.5	−0.12	3	−177
	180	0.7	−1.5	1.2	3.1	−0.3	−0.08	2	−155
Forget-me-not	20	2.7	−18.3	4.0	5.3	−0.1	−0.00	0	−172
	40	2.9	−11.4	3.2	4.5	−6.1	−0.43	25	−166
	60	1.5	−3.8	2.8	7.0	−1.5	−0.08	2	−158
	80	0.1	0.5	1.7	6.4	0.2	0.02	0	−11
Poinsettia	20	−8.4	−23.0	5.4	8.3	24.4	0.55	−26	160
	40	−3.2	−13.3	4.9	9.2	26.5	0.59	−20	166
	60	0.3	−7.3	5.1	8.6	23.3	0.55	−24	−178
	80	2.3	0.3	3.0	6.2	7.7	0.42	−14	−83

[a] Measured counterclockwise from north.
[b] Direction to which the current flows, measured counterclockwise from north.

are statistically unreliable because the standard deviation in this region is much larger than the mean and the records are relatively short.

The root-mean-square error in the estimation of the mean of a stationary series is given by (see, e.g., Lumley and Panofsky, 1964, p. 37)

$$\epsilon = \sigma(T/2\mathcal{T})^{-\frac{1}{2}}, \qquad (3.3)$$

where ϵ is the rms error of the mean estimate, σ the standard deviation of the signal, T the length of the time series, and $\mathcal{T}$ is the integral scale defined as half the area under the autocorrelation function. The quantity $T/2\mathcal{T}$ in (3.3) is the number of independent measurements, since the measurement at intervals greater than $2\mathcal{T}$ can be considered independent. The error bars ($\pm \epsilon$) for the northward mean at 20 m during CUE-1 are shown in Fig. 3. In these estimates the integral scale was taken to be about 2.5 days, which was arrived at from the extrapolated intercept at zero frequency of a number of spectra throughout the region. The uncertainty of the mean estimate near the shore is evident in this figure. The uncertainty, in fact, is even greater because of the nonstationarity of the series.

From Tables 1 and 2, it is apparent that u_{SD} consistently decreases with depth at all stations, whereas v_{SD} remains more or less constant with depth, although near the coast v_{SD} shows a small decrease with depth. The small decrease of v_{SD} at 5 m from the ocean bottom at Edelweiss (water depth 200 m) and Carnation (water depth 100 m) is accompanied by Ekman veering (Kundu, 1976). Fig. 4 shows a plot of u_{SD} and v_{SD} at 40 m depth as a function of the distance from the shore. The 40 m depth is chosen because it is an intermediate depth and because there is more complete data at this depth. It is evident that the fluctuation field is not far from being isotropic ($u_{SD} \approx v_{SD}$) at distances larger than 30 km, within which v_{SD} rises steeply whereas u_{SD} decreases as the coast is approached, as one should expect due to the boundary constraint. The alongshore excursion of the fluid particles is not so hampered until the effect of friction is felt, which apparently occurs in a layer whose width is less than 5 km. The results in Fig. 4 are qualitatively similar to the solutions from the numerical computation of shelf wave modes near the Oregon coast (Fig. 2 of Cutchin and Smith, 1973). For the first mode these solutions show a slow increase and
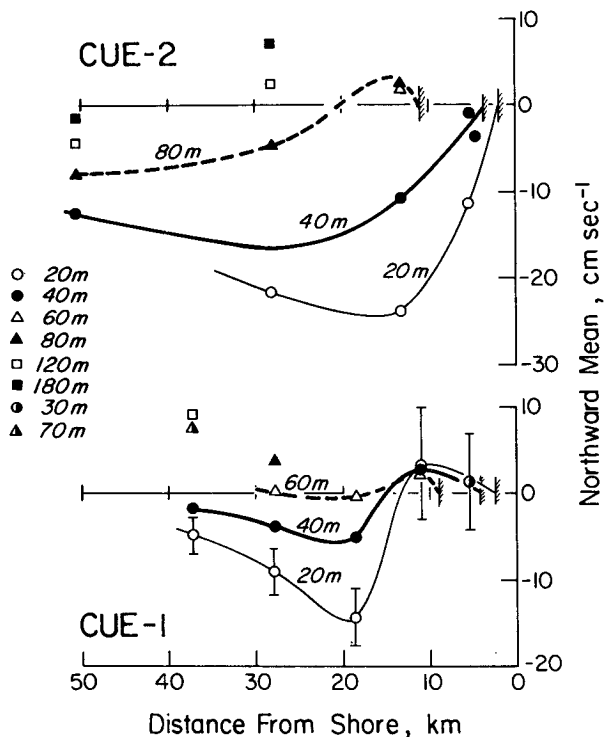
FIG. 3. The mean northward velocity $\bar{v}$ across an east-west cross section. The hatched lines denote the location of the intersection of the depth of measurement with the ocean bottom where the velocity is taken to be zero to satisfy the no-slip condition. The error bars are twice the standard deviations of the mean estimate of the 20 m current.

a subsequent decrease of the east-west amplitude, and a steep monotonic rise of the north-south amplitude as one approaches the coast. It may also be mentioned that an almost identical behavior is also obtained in a turbulent boundary layer parallel to a plate (Fig. 10.8 of Townsend, 1956), although the coastal dynamics are different from the dynamics of a turbulent boundary layer.

In Section 4 it will be demonstrated that the fluctuations seem to follow the direction of the local isobaths. It may, therefore, be more appropriate to look at the variation of the standard deviations in the so-called "principal" coordinate system, defined (see Section 4) by the directions along which the standard deviations are extremum, or alternatively, the directions along which the shear Reynolds stresses vanish. The standard deviations along the major (maximum standard deviation) and minor (minimum standard deviation) principal directions are also indicated in Fig. 4, where it is apparent that their nature of variation is similar to that in the east-north coordinate system.

It is of interest to determine the rate at which v_{SD} decreases offshore, and to examine the relation of v_{SD} with the local water depth. It follows from the theory of barotropic continental shelf waves (e.g., Buchwald

and Adams, 1968) that, for the nth shelf wave mode,

$$v \approx H^{-\frac{1}{2}}[\phi_{nx}+\tfrac{1}{2}(H_x/H)\phi_n],\qquad(3.4)$$

where $H(x)$ is the depth of water, the subscript x denotes the x derivative, ϕ_n is the solution to a Sturm-Liouville problem, and $\phi_n(x=0)=0$. These free wave modes, moreover, may be superimposed and used for the description of forced motion on the shelf (Gill and Schumann, 1974). Consequently, we might expect the magnitude of the alongshore velocity to decrease in the offshore direction at a rate which is not far from $H^{-\frac{1}{2}}$. By plotting the data for v_{SD} from CUE-1 and CUE-2 on a graph of log v_{SD} vs log H, we found that the slope of the mean line through these points gives $v_{\mathrm{SD}} \approx H^{-0.65}$, which is in qualitative agreement with the theoretical prediction.

4. Scatter plot and Reynolds stress

A number of features can be simply displayed by plotting so-called "scatter diagrams," in which the velocity vector (u,v) is plotted as a point in a hodograph plane at various times. Fig. 5 shows the scatter diagrams of the velocity fluctuations at the various CUE-1 and CUE-2 stations at a depth of 40 m (except for NH3 which is at the depth of 30 m), superimposed on a bathymetric map of the region. The mean was removed
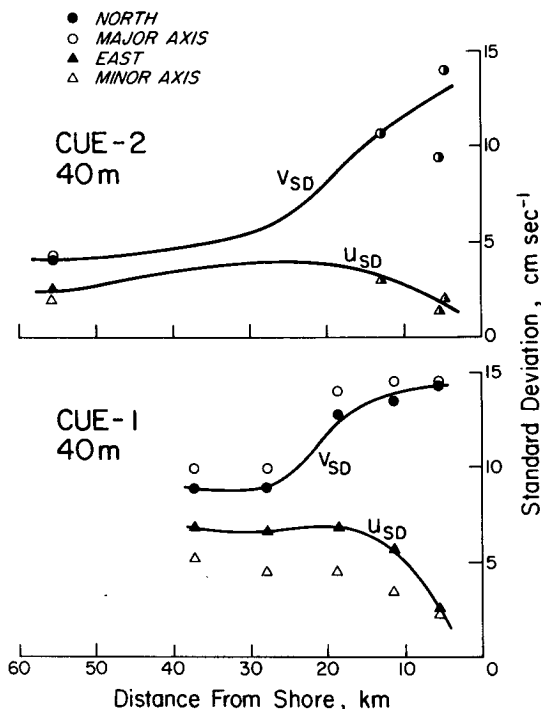

FIG. 4. The standard deviations at 40 m as a function of the distance from shore. The solid curves are drawn to pass through u_{SD} and v_{SD}. The values along the principal coordinates are indicated, but not joined. The half-solid symbols signify that ○ and ● (△ and ▲) are nearly superimposed, which will be the case if the principal axes are close to the east-north axes.
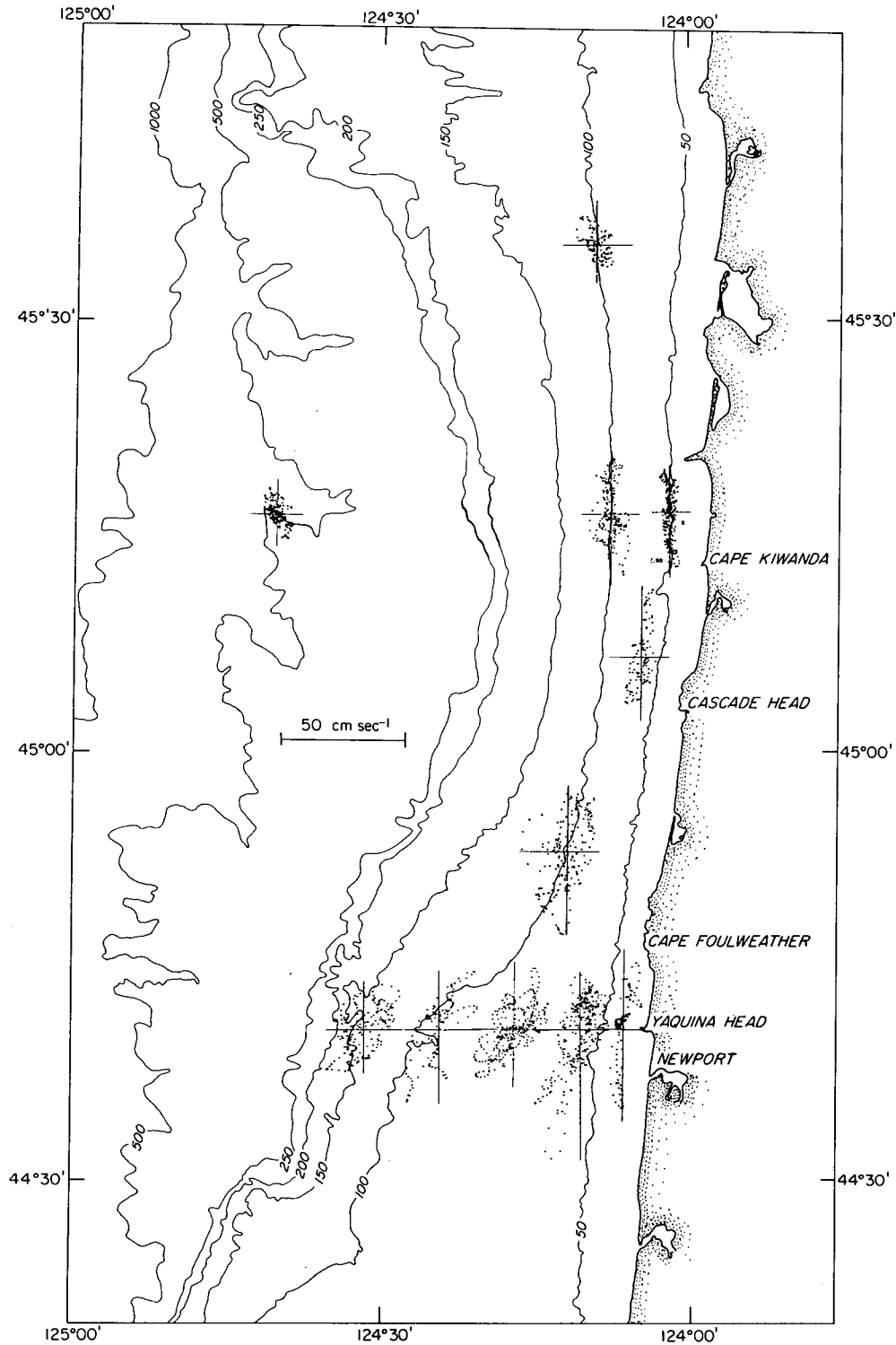
FIG. 5. Scatter diagrams of the 40 m velocity fluctuations at different stations during CUE-1 and CUE-2, superimposed on a bathymetric contour map.

from the data in these scatter plots; with the mean in, the center of gravity of the clusters will simply be shifted to the point $(\bar{u},\bar{v})$. The extent of one of these clusters in the x direction is a measure of u_{SD}, whereas the extent in the y direction is a measure of v_{SD}. The increase of v_{SD} and the decrease of u_{SD} as one approaches the coast is evident from these scatter plots.

Also evident is the "topographic steering" of the

fluctuations, that is, on the average the fluctuations roughly follow the direction of the local isobath. The isobaths seem to change direction across an east-west line off Cape Kiwanda, and the Reynolds stresses $\overline{u'v'}$ in the east-north coordinate system also change sign across the same line, being positive southward of it and negative northward (see also Table 2).

The direction of the polarization of the scatter plots is given by the eigenvectors (principal directions) of the Reynolds stress tensor $R_{ij} = \overline{q_i q_j}$, ($i = 1, 2$), where $q_1 = u'$ and $q_2 = v'$. It is easy to show that the principal directions θ_p are those along which the sum of the squares of the normal distances from the data points (u', v') is extremum, and are given by the two roots of

$$\tan 2\theta_p = 2\overline{u'v'}/(\overline{u'^2} - \overline{v'^2}). \qquad (4.1)$$

A simple graphical construction called the Mohr's circle, widely used in the theory of elasticity, can be used to find the principal axes and the maximum and minimum Reynolds stresses.

The dimensional and nondimensional Reynolds stresses and the direction of the principal axes at various stations are listed in Tables 1 and 2. The vertical distribution of the principal axis direction does not seem to follow any pattern, but the intuitive expectation that the bottom currents may be more topographically steered than the upper currents does not seem to be correct.

The fact that the Reynolds stresses in the region are influenced by the bottom topography raises the question of whether this has any relevance on the exchange of energy between the fluctuations and the mean flow. It is well known that the mean local transfer of energy from the mean flow to the fluctuation is given by $-\overline{u'_i u'_j} \; (\partial \bar{u}_i / \partial x_j)$ in Cartesian tensor notation. This term can be active even in two-dimensional flows where the mechanism of vortex stretching is absent, and under special circumstances can cause transfer of energy from the fluctuations to the mean flow, for example in the phenomenon of frictionally induced streaming near the boundary over which a wave motion propagates (Phillips, 1969, p. 38). A careful analysis of the effect of bottom topography on the direction of energy transfer, including frequencies other than those reported here, is not pursued here. However, note that in the present region the horizontal eddy coefficient of viscosity obtained by dividing the mean velocity gradient by the Reynolds stress has different signs at different locations, and it is not possible to cite an approximate value to be used in (laminar-type) theories.

5. Spatial correlations

To determine how the currents in the region are spatially related, the correlation coefficients of u and v as a function of the distance of separation were calculated

at different depths. The correlation coefficient, say for the u component, between two stations x_1 and x_2 is defined as

$$r_u(x_1, x_2) = \overline{u'(x_1, t) u'(x_2, t)} / [\overline{u'^2}(x_1, t) \overline{u'^2}(x_2, t)]^{\frac{1}{2}}. \qquad (5.1)$$

The correlation coefficients at 40 m are shown in Fig. 6. In computing these coefficients, the largest common length of record was taken, but the months of September and October were ignored. The correlation coefficient as a function of the east-west separation is shown in Fig. 6a, in which the CUE-1 result is centered at NH20 and the CUE-2 result at *Forsythia*. Fig. 6b shows the correlation coefficients as a function of the alongshore separation, where the stations are approximately on the 100 m isobath line and roughly north-south; the CUE-1 results are centered at DB7 while the CUE-2 results are centered at *Forget-me-not*. A typical standard error of these correlation coefficients was estimated, by an expression similar to (3.3), to be about ±0.3. Note that, for both CUE-1 and CUE-2, the correlation coefficients for v are much higher than those for u, both for approximately alongshore as well as east-west separations. In fact, they seem to define different space scales for the u and v components. [This is contrary to a turbulent boundary layer where the so-called lateral and longitudinal correlation functions, although somewhat different, show correlation scales of the same order of magnitude; see Comte-Bellot (1965).] The reason may be the following: It is probably a reasonable assumption that the coastal region under consideration has a great deal of forced or free shelf wave activity, and some "turbulence" superimposed on it. The shelf waves generate a much larger v than u [see, for example, the numerical computations in Cutchin and Smith (1973)]. Therefore, these organized, wave-induced v components are able to rise above the background turbulence level and show a larger correlation scale, whereas the wave-induced u components get somewhat mixed with the background turbulence and display a smaller correlation length.

Note that the correlation of the u components as a function of the alongshore separation goes to negative values in CUE-2. This is evidently due to topographic steering, which causes the u fluctuations at *Forget-me-not* to be opposite in sign to that at *Iris* and *Poinsettia*. To demonstrate this, we computed the correlation coefficients of the fluctuations along the major and minor principle axes. The results are also indicated in Fig. 6, where it is seen that the correlation coefficients of the fluctuations along the minor axes, for stations separated alongshore, do not go to significant negative values. A comparison of the two sets of correlations, i.e., along either the east-north or the minor-major axes, in Fig. 6 reveals the following facts: 1) r_v is generally of the same order of magnitude as the correlation of the fluctuations along the major axes, and 2) r_u is generally larger in absolute value than the correlations along the minor
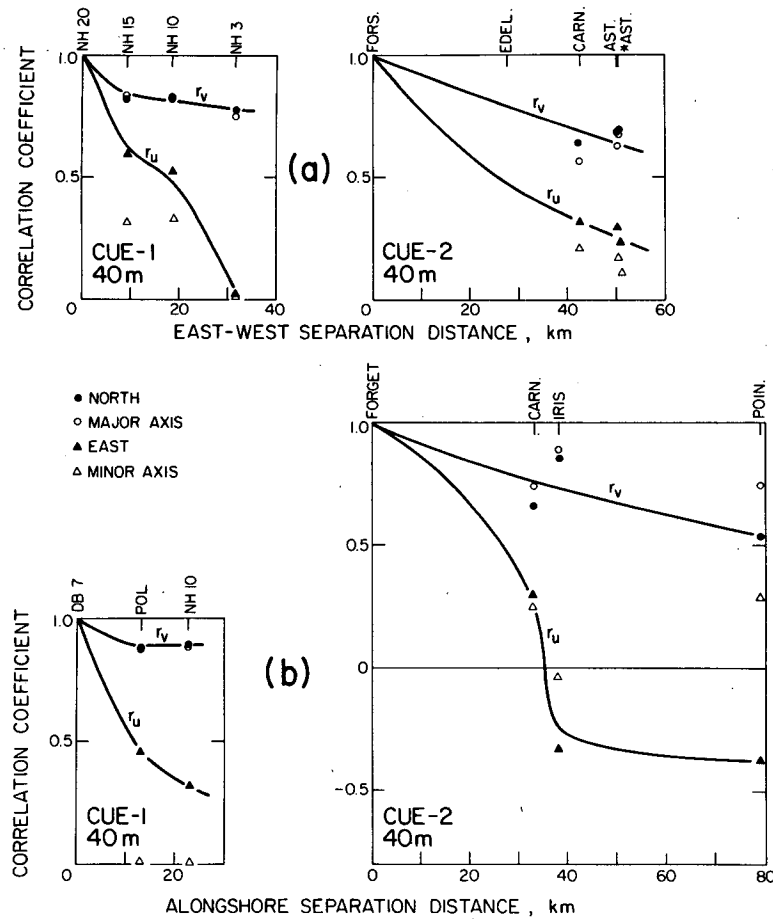
FIG. 6. Correlation coefficients at 40 m. The solid curves are passed through the values along the east-north axes. The correlation coefficient of fluctuations along the principal axes are indicated, but not joined.

axes. The latter is due to the fact that the u fluctuations carry a part of the major axis fluctuations.

The correlation functions were also computed for the

FIG. 7. Correlation coefficients at *Carnation* and DB7 as a function of vertical separation.

CUE-2 data at 20, 60 and 80 m depths, those for the CUE-1 measurements not being computed for lack of sufficient data. The behavior at these depths is similar to that at 40 m, and therefore is not shown. In general, however, the velocities at the upper depths showed a somewhat smaller correlation than those at the lower depths, presumably due to decrease of "turbulence" and baroclinic effects (Kundu et al., 1975) with depth.

Note from Fig. 6b that for the CUE-1 data r_v essentially levels out at about 0.9 within the Oregon coast region. This is consistent with the finding of Huyer et al. (1975) that $r_v = 0.86$ between the 60 m current at NH10 and the 66 m current at a similar station, UWIN, off the coast of Washington with an alongshore separation of 200 km. This high r_v, however, is not evident for the CUE-2 measurements. In the next section we shall also see that the mean alongshore propagation speed of the current fluctuations during CUE-2 was much smaller than that during CUE-1, although both were northward. This smaller propagation speed might be responsible for an increased dissi-
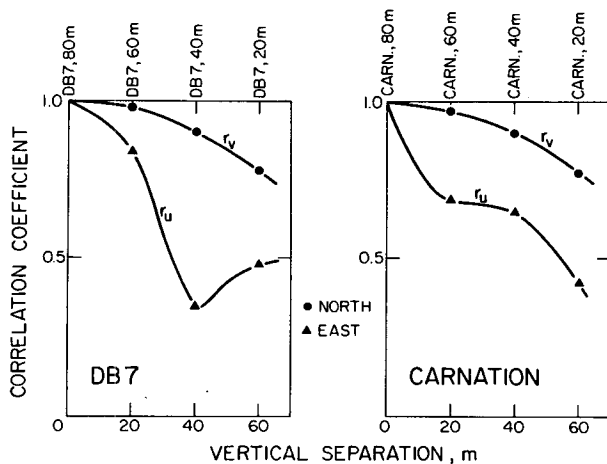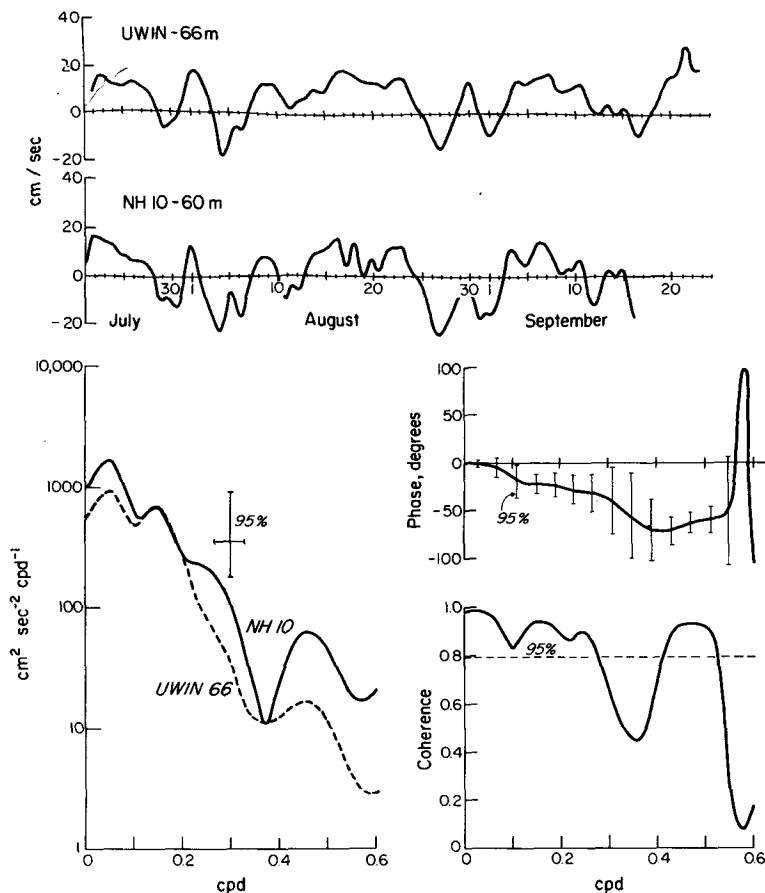
FIG. 8. Time series and cross spectra of v at NH10 (60 m) and UWIN (66 m).
Negative phase angle corresponds to NH10 leading UWIN.

pation of the signal as it propagates alongshore, resulting in a smaller alongshore correlation during 1973.

The correlation coefficient as a function of vertical separation is displayed in Fig. 7 for DB7 and *Carnation*, where again the high correlation of the v fluctuations can be seen.

6. Alongshore propagation speed

A plot of the time series of the northward component of the currents at two 1972 stations separated by an alongshore distance of 200 km is shown in the upper panel of Fig. 8; those for some 1973 stations also separated alongshore are shown in Fig. 9. A careful comparison of the peaks and valleys in these series clearly reveals the northward propagation of the signals along the coast.

Based on cross-spectral analyses, quite a few computations have been reported (Mooers and Smith, 1968; Cutchin and Smith, 1973; Huyer *et al.*, 1975) on the propagation speed of the currents near the Oregon-Washington coast. They have been reported as northward as well as southward, identified with different frequencies (between 0.15 and 0.45 cpd), and accorded

different propagation speeds (between 200 and 2000 km day^{-1}). The most recent study is that of Huyer *et al.* (1975) who examined the alongshore coherence of low-frequency currents over the continental shelf off Oregon and Washington in the summer of 1972. We utilize here some of the same measurements reported in Huyer *et al.* (1975), but because of the uncertainties involved in the spectral calculations of these short time series, especially the error bounds on the phase angle calculations, it was decided to attempt a similar computation in the time domain, where the confidence intervals are much smaller because no frequency resolution is sought.

We define the "lagged" correlation function as

$$r(\mathbf{x_1},\mathbf{x_2},\tau) = \overline{v'(\mathbf{x_1},t)v'(\mathbf{x_2},\,t+\tau)}/[\overline{v'^2}(\mathbf{x_1},t)\overline{v'^2}(\mathbf{x_2},t)]^{\frac{1}{2}}. \quad (6.1)$$

The v component of the velocity is used here, because it shows higher correlation and therefore less contamination due to "noise." If τ_m is the lag which gives the maximum correlation, then the propagation speed in the direction of $\mathbf{d} = \mathbf{x_1} - \mathbf{x_2}$ is $|\mathbf{d}|/\tau_m$, the sense being determined from the sign of τ_m.
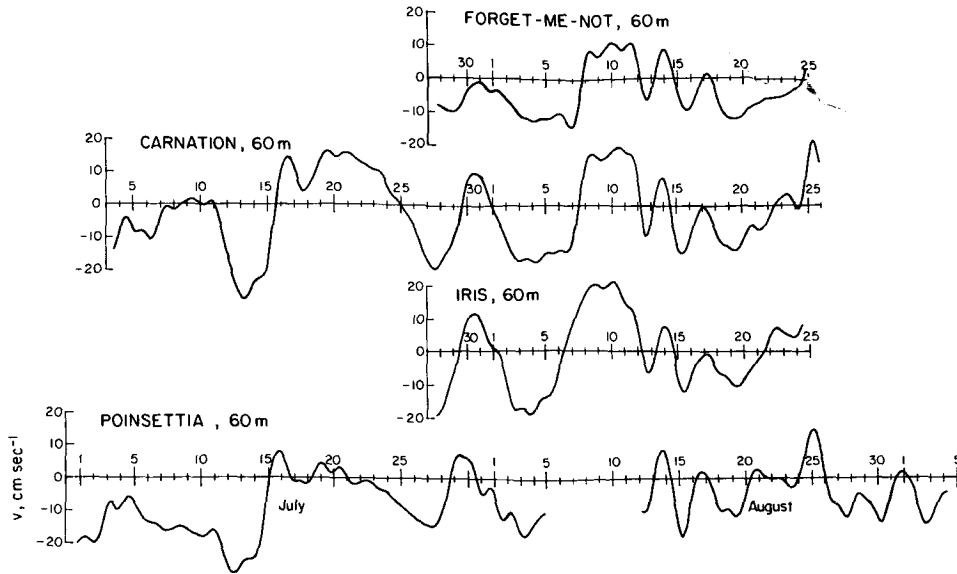
FIG. 9. Time series of v at various CUE-2 stations separated alongshore.

For this particular computation, the time series were not decimated to 6 h values after low-passing through the 40 h filter. Instead, they were filtered in the same manner but the hourly values were saved so as to obtain a time resolution of 1 h.

For the 1972 measurements, the propagation speed was estimated from the time lag for maximum correlation between the 60 m current at NH10 and the 66 m current at UWIN, which were separated by a large distance of 200 km. A time lag of $\tau_m=9$ h was found, with NH10 leading (Fig. 10a), so that the mean propagation is northward with speed $c\approx 500$ km day^{-1} (~ 5.8 m s^{-1}) for 1972. Although no other station was used for this computation because the alongshore separ-

ation within the CUE-1 array was small (<23 km), a plot of τ_m versus the alongshore separation d for the CUE-1 stations is also indicated in Fig. 10a, where again the southern stations lead the northern stations. Note that the time lag within the CUE-1 array came out to be about an hour greater than those expected from $c=500$ km day^{-1}. However, keeping in mind the fact that we only retained a time resolution of 1 h, and the various other uncertainties involved, we do not think that this one hour difference is significant enough to imply that the signals are propagating slower off the coast of Oregon, and accelerating on the way up the coast.

Without the spectral decomposition, no particular
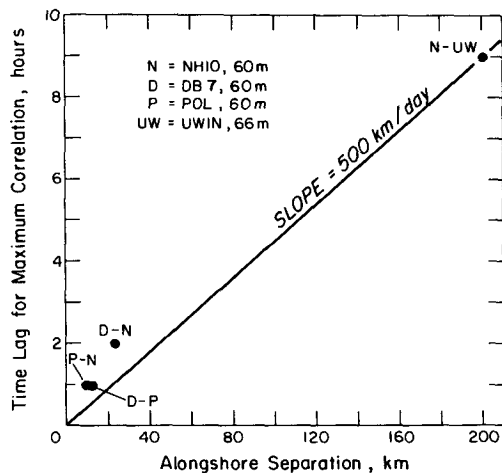
(a)
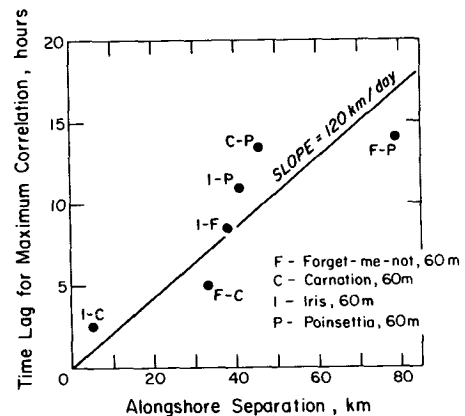
(b)

FIG. 10. The lag time of maximum correlation versus the alongshore distance of separation for 1972 (a) and 1973 (b).

frequency can be singled out, and one can only say that the "energetic" signals propagate at the mean phase speeds quoted, whatever their frequency. However, more can be inferred about the propagation from an examination of the time series of the north-south fluctuations at NH10 and UWIN (Fig. 8). The southern station (NH10) shows a good deal of high-frequency ($\omega \approx 0.5$ cpd), 2-day period motion, whose amplitude is much smaller at the northern station (UWIN). Otherwise, in the range $0 < \omega < 0.4$ cpd, the signals are roughly identical in form, simply phase shifted by a few hours. This means that these frequencies traveled with roughly the same speed, that is, the propagation is approximately nondispersive. It is easy to see that in such a case the magnitude of the phase angle should increase linearly with frequency if a cross-spectral analysis were carried out. To show this, suppose that the phase difference between two stations separated by a distance L at frequency ω is $\phi(\omega)$ [deg]. Then the wavelength is $\lambda(\omega) = 360L/\phi$, so that the propagation speed is $c(\omega) = \omega\lambda = 360L\omega/\phi$. Therefore, for c to be independent of ω, we must have ϕ proportional to ω.

A cross-spectral analysis of the v components of the fluctuations of the 60 m current at NH10 and the 66 m current at UWIN was also performed, the results of which are displayed in the lower panel of Fig. 8. The two autospectra show energy throughout the 0–0.4 cpd range. In addition, the NH10 autospectrum show a large peak at 0.46 cpd (~ 2 day period), which was virtually absent from the autospectrum of UWIN, a feature already noted from the visual inspection of the time series. The signals were also coherent throughout almost the entire range of 0 to 0.5 cpd (with a low only at about 0.35 cpd); the phase angle ϕ was very nearly linear throughout the same range also, signifying a roughly nondispersive propagation. From the phase spectrum, the speed of propagation comes out to be about 500 km day^{-1} ($\phi \approx 40°$ at $\omega = 0.3$ cpd; with $L = 200$ km, this gives $c \approx 540$ km day^{-1}), agreeing with the time-lagged correlation computation. Huyer et al. (1975) also estimated a similar phase speed of 575 km day^{-1} at 0.16 cpd from the same data.

For the CUE-2 data, the time lag for maximum correlation is plotted against the distance of separation in Fig. 10b, where all the stations were at a depth of 60 m and were separated in the alongshore direction. Again it was found that τ_m always came out to be positive if Station 2 was northward of Station 1 [see (6.1)], signifying a northward propagation. The mean speed of propagation, given by the slope of the straight line passing through the points in Fig. 10b, is $c \approx 120$ km day^{-1} (~ 1.4 m s^{-1}) for 1973. From the size of the scatter in Fig. 10b the accuracy of the above estimate seems to be about $\pm 30\%$. No cross-spectral calculations could be performed because of the small common length of the series.

It may be noted that the mean velocities of 500 and

120 km day^{-1} are close to those calculated by Cutchin and Smith (1973) for the first and second mode free barotropic continental shelf waves in the low-frequency or nondispersive range. From the dispersion curves in Cutchin and Smith (1973), the first mode appears to be nearly nondispersive for $\omega < 0.35$ cpd (wavelength $\lambda > 1000$ km), whereas the second mode has a nondispersive behavior for $\omega < 0.28$ cpd ($\lambda > 400$ km).

The results from 1972 appear to indicate that all the low-frequency current fluctuations for $\omega < 0.3$ cpd propagate northward nondispersively at a mean velocity of 500 km day^{-1}. This is consistent with the current fluctuations at the relevant frequencies existing in the form of first mode continental shelf waves. These modes might be propagating northward, at the first mode wave speed, as free waves. The idea of free waves, however, does not fit well with the reasonably high correlation of the alongshore current velocities with the local alongshore component of the wind stress τ_w. In addition, in Kundu et al. (see their Table 7) it was shown that in 1972 the barotropic component of the alongshore current at DB7 was very highly coherent with τ_w at 0.14 cpd and that the corresponding value of the phase differences (between τ_w and u, τ_w and v, and u and v) at this frequency were consistent with resonant forcing by the winds. A resonant condition may exist if a component of the wind stress travels northward as a wave with the phase velocity and wavelength of a free continental shelf wave mode. Moreover, accompanying this high coherence and phase relation at 0.14 cpd is a peak in the autospectrum of v, evident in Fig. 8, which also supports the idea that energy is somehow more efficiently transferred to the currents at this frequency.

To investigate further the concept of resonant forcing, we have analyzed the data on coastal winds from Newport, Ore., near the NH line, and from Westport, Wash., near UWIN (see also Huyer et al., 1975). A correlation of the northward component of these winds showed a time lag for maximum correlation of 2.5 h, the southern station leading. The maximum correlation coefficient between the two winds was quite high (0.83), but the amplitude of the fluctuation at the northern station was nearly half that at the southern station. This time lag (2.5 h) is much shorter than that for the currents (9 h). A cross-spectral analysis of the northward component of these winds showed a high (>0.9) coherence for $0 < \omega < 0.16$ cpd with an accompanying phase difference which was nearly zero for $\omega < 0.12$ cpd but which had a value of 20° (Newport leading) at $\omega \approx 0.14$ cpd. This implies a phase velocity of ~ 500 km day^{-1} for the wind at 0.14 cpd. A similar result was found at 0.16 cpd by Huyer et al. (1975).

It appears, therefore, that although most of the fluctuations at the energetic frequencies in the alongshore component of the wind were about simultaneous at the two stations, the $\omega \approx 0.14$ cpd component of the wind propagated at a mean speed of about 500 km day^{-1},

which is close to the speed of propagation of all the low-frequency fluctuations in the currents and is close to the nondispersive phase velocity of a first mode continental shelf wave. This gives further support to the concept of resonant forcing of a first mode shelf wave at $\omega \approx 0.14$ cpd. It does not, however, explain the propagation of the current fluctuations at the other frequencies at approximately the same mean velocity, and the possible existence of these fluctuations in the form of a first mode shelf wave. Several explanations for the latter behavior are possible. For example, the response to an impulsive (strong and short-lived, wind event type) forcing will be composed, after the forcing has abated, of a set of free wave modes. The lowest mode should be expected to have the largest amplitude (Gill and Schumann, 1974) and also, perhaps, to persist longer than the higher modes. The first mode, therefore, could dominate the alongshore current structure. Alternatively, it is still possible for a resonance mechanism to exist at frequencies other than about 0.14 cpd, and to produce a forced response with the free wave propagation velocity, if the wind stress is in a standing wave configuration and has an appropriate traveling wave component of τ_w (see, e.g., Kundu et al., 1975). These possibilities, however, cannot be resolved here.

The reason for the occurrence of the smaller mean propagation speed of 120 km day^{-1} during CUE-2 in 1973 is not understood. Although this speed is similar to that of the second mode free shelf wave, the second mode has a zero crossing for v in the offshore direction, which for the case studied by Cutchin and Smith (1973) was found to be at about 40 km from the coast. If the currents are primarily in the form of a second mode then measurements from either side of the zero crossing should be negatively correlated. However, we find only positive correlation of the v components in an offshore direction, up to a separation of about 52 km (Fig. 6), which does not seem to indicate the presence of a second mode. On the other hand, the location of the zero crossing is not exactly known, because the computations in Cutchin and Smith (1973) were made on the basis of the bathymetry across DB7, and it is not certain to what extent the alongshore variations in bathymetry influence the mode shapes.

In any case, the alongshore propagation problem deserves further study with more alongshore measurements and with measurements at greater alongshore separation distances. The high correlation of the alongshore currents over the shelf with sea level at the coast (Section 7) indicates that sea level measurements along the coast might provide an accurate and accessible tool to pursue these questions.

7. Empirical orthogonal decomposition

A decomposition of the velocity fields at *Carnation* and DB7, into the dynamic modes and into the "empirical orthogonal functions," was performed by Kundu

et al. (1975). It was found that the vertical empirical mode shapes were very similar to the dynamic mode shapes and, among other things, that the amplitude of the first baroclinic mode at DB7 was correlated with the temperature fluctuations at 40 m at the same station. It is important to determine whether this kind of correlation between the baroclinic velocities and temperature is observed at other stations, and whether these baroclinic fluctuations propagate along the coast. Such a modal decomposition of the velocity field at other stations has therefore been carried out. A brief outline of the method is given first [for more details see Kundu et al. (1975)].

Let $v(\mathbf{x}_i, t_k)$ denote the value of a scalar variable at time t_k $(k=1, 2 \ldots K)$ and location $\mathbf{x}_i$ $(i=1, 2, \ldots N)$. One can define a real, symmetric and positive definite matrix of correlation coefficients as

$$R(\mathbf{x}_i, \mathbf{x}_j) = \frac{1}{K} \sum_{k=1}^{K} v(\mathbf{x}_i, t_k) v(\mathbf{x}_j, t_k), \qquad (7.1)$$

and find its real eigenvectors $\phi_n(\mathbf{x}_j)$ and positive eigenvalues λ_n

$$\sum_{i=1}^{N} R(\mathbf{x}_i, \mathbf{x}_j) \phi_n(\mathbf{x}_i) = \lambda_n \phi_n(\mathbf{x}_j), \qquad n=1, \ldots, N. \quad (7.2)$$

The eigenvectors, which satisfy the orthogonality condition

$$\sum_{i=1}^{N} \phi_n(\mathbf{x}_i) \phi_m(\mathbf{x}_i) = \delta_{nm}, \qquad (7.3)$$

are called "empirical orthogonal functions" (mode shapes). The eigenvalues λ_n are the time average energy (variance) in the various modes, and the sum of the eigenvalues add up to the total energy. The set $\{\phi_n\}$ forms a new basis in the vector space in which the data points can be assumed to be situated, so that

$$v(\mathbf{x}_i, t_k) = \sum_{n=1}^{N} E_n(t_k) \phi_n(\mathbf{x}_i), \qquad (7.4)$$

where

$$E_n(t_k) = \sum_{i=1}^{N} v(\mathbf{x}_i, t_k) \phi_n(\mathbf{x}_i). \qquad (7.5)$$

It can be shown that the modal amplitudes $E_n(t_k)$ are uncorrelated in time.

The results of the empirical orthogonal decomposition by stations, where $\mathbf{x}_i$ in (7.1)–(7.5) stand for various depths z_i at one geographic location, are shown in Table 3. In this table, the normalized correlation coefficients are denoted by the angle brackets. For example,

$$\langle E_{1u} \tau_w \rangle = \overline{E_{1u} \tau_w} / E_{1u\mathrm{SD}} \tau_{w\mathrm{SD}},$$

TABLE 3. Empirical orthogonal decomposition at various stations.

Station	Depth (m)	U component								V component							
		ϕ_{1u}	λ_{1u} (cm² s⁻²)	Per-cent	$\langle E_{1u}\tau_w\rangle$	ϕ_{2u}	λ_{2u} (cm² s⁻²)	Per-cent	$\langle E_{2u}\tau_w\rangle$	ϕ_{1v}	λ_{1v} (cm² s⁻²)	Per-cent	$\langle E_{1v}\tau_w\rangle$	ϕ_{2v}	λ_{2v} (cm² s⁻²)	Per-cent	$\langle E_{2v}\tau_w\rangle$
Aster	20	0.99	16.3	87.9	-0.14	0.15	2.3	12.1	0.33	0.81	232.0	95.1	0.55	0.59	12.0	4.9	-0.31
	40	0.15				-0.99				0.59				-0.81			
Carnation	20	0.79				0.61				0.43				0.81			
	40	0.42	29.3	68.8	-0.15	-0.48	8.9	20.1	0.36	0.50	420.2	91.1	0.54	0.14	30.0	6.4	-0.35
	60	0.37				-0.54				0.56				-0.34			
	80	0.24				-0.32				0.50				-0.45			
Edelweiss	20	0.92				0.29				0.32				0.81			
	80	0.25				-0.20				0.44				0.23			
	120	0.25	15.3	51.9	-0.24	-0.30	9.0	30.3	0.17	0.51	99.6	73.5	0.42	0.01	30.0	22.1	0.39
	180	0.12				-0.51				0.50				-0.40			
	195	0.10				-0.73				0.44				-0.37			
Forsythia	40	0.86				0.27				0.57				0.76			
	80	0.39	7.5	66.9	-0.16	0.19	1.6	14.7	-0.12	0.51	40.7	85.1	0.47	-0.03	4.1	8.7	0.30
	120	0.22				-0.76				0.49				-0.38			
	180	0.24				-0.56				0.43				-0.53			
Forget-me-not	20	0.71				0.68				0.36				0.84			
	40	0.52	26.3	71.9	0.05	-0.33	5.6	15.2	0.17	0.39	114.6	83.0	0.52	0.24	17.8	12.9	0.17
	60	0.43				-0.51				0.62				-0.39			
	80	0.21				-0.41				0.57				-0.28			
Poinsettia	20	0.54				0.66				0.46				0.83			
	40	0.61	55.5	80.5	0.32	0.08	7.5	11.0	0.26	0.49	145.6	91.5	0.69	-0.20	7.7	4.9	0.07
	60	0.49				-0.45				0.55				-0.05			
	80	0.32				-0.59				0.49				-0.52			
Iris	20	0.56				0.83				0.52				0.74			
	40	0.75	11.5	56.8	0.14	-0.51	6.7	33.2	0.36	0.64	360.8	94.5	0.32	0.00	15.4	4.0	-0.38
	60	0.36				-0.24				0.57				-0.68			
DB7	20	0.52				0.23				0.43				0.67			
	40	0.63	79.7	73.8	0.27	0.52	19.6	18.1	-0.35	0.51	684.8	92.0	0.68	0.37	51.1	6.9	0.18
	60	0.48				-0.48				0.54				-0.39			
	80	0.32				-0.67				0.51				-0.52			
NH6	20	0.75				0.66				0.70				0.70			
	40	0.60	74.6	90.0	0.59	-0.72	7.2	8.7	-0.03	0.57	477.1	95.7	0.68	-0.45	18.7	3.8	-0.01
	60	0.28				-0.22				0.43				-0.55			
NH10	20	0.60				0.65				0.55				0.79			
	40	0.65	107.2	93.2	0.34	-0.06	5.2	4.5	-0.37	0.63	404.4	92.8	0.42	-0.19	25.1	5.8	-0.26
	60	0.47				-0.76				0.55				-0.58			
NH15	40	0.63				0.74				0.71				0.60			
	60	0.62	122.3	90.2	0.31	-0.28	10.1	7.5	-0.07	0.62	178.1	92.2	0.51	-0.31	12.3	6.4	-0.10
	80	0.47				-0.62				0.32				-0.74			
NH20	20	0.71				0.47				0.48				0.52			
	40	0.60	102.6	91.8	0.08	-0.01	4.2	3.7	-0.47	0.51	185.5	81.0	0.50	0.40	36.8	16.1	-0.51
	70	0.36				-0.88				0.50				-0.12			
	120	0.10				-0.08				0.52				-0.75			

where τ_w is the northward component of the wind stress and E_{1u} the amplitude of the first empirical mode for the u component. The eigenfunctions are computed for the largest common time period for the group of records at each station (Fig. 2). The time mean was removed from the data series in each case. First note that ϕ_{1v}, the first mode for the v component, is fairly depth-independent at many stations. However, at stations near the coast ($Aster$, NH6), and also at NH15, this mode shape corresponds to stronger fluctuations near the surface, whereas at $Forget-me-not$ it reveals stronger fluctuations near the bottom. This mode accounts for nearly 90% of the energy at most stations, and is fairly well correlated with the wind stress. The second mode

ϕ_{2v} resembles a dynamic baroclinic mode, with a zero crossing somewhere in depth, and accounts for roughly 5–10% of the energy. Except for a few stations, its amplitude E_{2v} has a poor correlation with the wind stress in general.

The first mode shape for the east-west fluctuations, ϕ_{1u}, always has larger values near the surface, and accounts for typically 60–80% of the energy. The second mode ϕ_{2u} has a zero crossing and accounts for about 10–15% of the energy. Both modes have poor correlation with the wind stress.

To find out whether these modal amplitudes are spatially coherent, the correlation coefficients of E_1 and E_2 were computed between the different stations for

TABLE 4. Correlation coefficients of the modal
amplitude between stations

Station pair	Correlations of			
	E_{1v}	E_{2v}	E_{1u}	E_{2u}
Carnation & Aster	0.88	0.20	−0.03	−0.12
Edelweiss & Aster	0.73	0.21	−0.08	0.15
Forsythia & Aster	0.72	−0.15	0.32	−0.29
Forget-me-not & Carnation	0.81	0.13	0.09	0.30
Forget-me-not & Iris	0.87	−0.42	−0.26	0.14
Carnation & Iris	0.96	−0.54	−0.14	−0.12
Aster & Iris	0.92	−0.25	0.09	−0.16

the CUE-2 data (Table 4). It is seen that the first modal amplitudes for the v component are well correlated within the region. Since this mode accounts for most of the energy in the data, a propagation speed of this mode was not computed because it would be roughly the same as that of the signal at 60 m, already computed in Section 6. Time-lagged correlation coefficients were computed between the E_{2v} at the various CUE-2 stations separated alongshore. However, no consistent result was found and no evidence of alongshore propagation of the second empirical mode was detected.

The second modal amplitude E_{2v} at DB7 was found to have a good correlation with the local temperature at 40 m in Kundu et al. (1975), whereas no such correlation at Carnation was found in that work. In the present study, we have tried to detect this kind of correlation at several other stations, but found none. An examination of the hydrographic data of Halpern and Holbrook (1972) and Holbrook and Halpern (1974), taken during the CUE-1 and CUE-2 respectively, shows that DB7 was one of a very few stations where there was a mid-depth vertical temperature gradient of the same sign throughout the upwelling season. This could explain the presence of correlation at DB7 and its absence at other stations.

An empirical orthogonal decomposition of the velocity field on a two-dimensional east-west plane was also performed. The results are shown in Table 5. Fifteen current meter records were used, so that the total number of modes was 15. However, a single mode explains about 74% of the energy for the v component. The first modal structure ϕ_{1v} shown in Table 5 demonstrates the fact that the simultaneous current fluctuations decrease in magnitude away from the coast but are roughly depth-independent at one station, i.e., the fluctuations are roughly in the form of a barotropic coastal jet. The time series for the wind stress, sea level, and E_{1v} of this decomposition are displayed in Fig. 11, where the strong correlation of E_{1v} with the sea level (0.82) and the somewhat weaker correlation of E_{1v} with the wind stress are evident.

8. Complex empirical orthogonal decomposition

Because of the geophysical importance, it is of interest to extend the empirical orthogonal decomposition technique to a group of two-dimensional vector time series.[2] The formulation is identical to that for scalar series outlined in Section 7, only minor modifications being necessary to generalize it for vectors. Let

$$w(\mathbf{x}_i, t_k) = u(\mathbf{x}_i, t_k) + iv(\mathbf{x}_i, t_k) \qquad (8.1)$$

denote the two-dimensional velocity vector at time t_k $(k = 1, \ldots K)$ and location $\mathbf{x}_1$ $(i = 1, \ldots N)$. We define a complex matrix of correlation coefficients

$$R(\mathbf{x}_i, \mathbf{x}_j) = \frac{1}{K} \sum_{k=1}^{K} w^*(\mathbf{x}_i, t_k) w(\mathbf{x}_j, t_k), \qquad (8.2)$$

and find its eigenvectors $\phi_n(\mathbf{x}_i)$, and eigenvalues λ_n, defined by

$$\sum_{i=1}^{N} R(\mathbf{x}_i, \mathbf{x}_j) \phi_n(\mathbf{x}_i) = \lambda_n \phi_n(\mathbf{x}_j), \quad n = 1, \ldots N. \qquad (8.3)$$

[2] The idea was given to us in a private communication by Dr. C N. K. Mooers who has evidently developed a similar extension.

TABLE 5. Empirical orthogonal decomposition on an east-west plane during CUE-2.

	U component								V component							
	ϕ_{1u}	λ_{1u} (cm² s⁻²)	Per-cent	$\langle E_{1u}\tau_w\rangle$	ϕ_{2u}	λ_{2u} (cm² s⁻²)	Per-cent	$\langle E_{2u}\tau_w\rangle$	ϕ_{1v}	λ_{1v} (cm² s⁻²)	Per-cent	$\langle E_{1v}\tau_w\rangle$	ϕ_{2v}	λ_{2v} (cm² s⁻²)	Per-cent	$\langle E_{2v}\tau_w\rangle$
Aster 20	0.15				0.09				0.47				−0.42			
Aster 40	0.12				0.16				0.37				−0.22			
Carn 20	0.44				0.15				0.31				0.65			
Carn 40	0.50				−0.15				0.33				0.38			
Carn 60	0.53				−0.29				0.43				0.07			
Carn 80	0.27				0.21				0.39				−0.03			
Edel 20	0.20				0.82				0.13				−0.35			
Edel 80	0.23	25	32	−0.46	0.10	18	23	−0.37	0.15	598	74	0.39	−0.12	85	11	−0.57
Edel 120	0.16				0.13				0.14				−0.01			
Edel 180	0.10				0.01				0.10				0.10			
Edel 195	0.17				−0.06				0.09				0.08			
Forsyth 40	0.00				0.23				0.11				−0.15			
Forsyth 80	−0.07				0.15				0.07				−0.11			
Forsyth 120	0.00				−0.07				0.07				−0.01			
Forsyth 180	0.02				−0.06				0.07				0.08			

Because the correlation matrix is Hermitian, that is $R(x_i,x_j) = R^*(x_j,x_i)$, the complex eigenvectors satisfy the orthogonality condition

$$\sum_{i=1}^{N} \phi_n^*(x_i)\phi_m(x_i) = \delta_{nm}, \qquad (8.4)$$

and the eigenvalues λ_n are real. Moreover, because of the Schwartz inequality

$$R(x_i,x_i) \, R(x_j,x_j) \geqslant R^*(x_i,x_j) \, R(x_i,x_j), \qquad (8.5)$$

the eigenvalues are also positive.

These eigenvectors ϕ_n may be called the "complex empirical orthogonal modes." If the data are expanded in terms of them,

$$w(x_i,t_k) = \sum_{n=1}^{N} E_n(t_k)\phi_n(x_i), \qquad (8.6)$$

then the complex amplitudes $E_n(t_k)$ are given by

$$E_n(t_k) = \sum_{i=1}^{N} \phi_n^*(x_i)w(x_i,t_k). \qquad (8.7)$$

It follows that

$$\sum_{k=1}^{K} E_n^*(t_k)E_m(t_k) = \lambda_n\delta_{nm}, \qquad (8.8)$$

so that the amplitudes of two different modes are uncorrelated in time, and that the eigenvalues are the time mean energy in the various modes. The sum of the eigenvalues equals the total energy:

$$\frac{1}{K}\sum_{k=1}^{K}\sum_{i=1}^{N} w^*(x_i,t_k)w(x_i,t_k) = \frac{1}{K}\sum_{k=1}^{K}\sum_{n=1}^{N} E_n^*(t_k)$$

$$\times E_n(t_k) = \sum_{n=1}^{N}\lambda_n. \qquad (8.9)$$

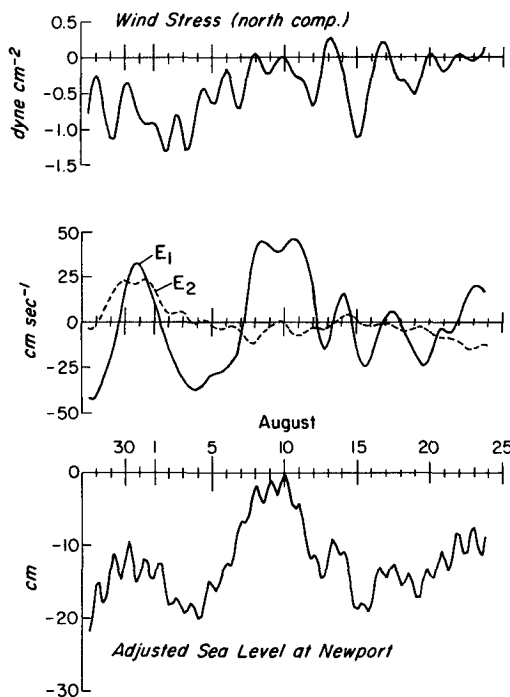This method was applied to the CUE-1 and CUE-2

FIG. 11. Time series of wind stress, E_{1v} and E_{2v} of the two-dimensional section, and sea level at Newport, 1973.

data with the mean removed, some of the results of which are displayed in Table 6. The eigenfunctions were computed using the largest common record length (Fig. 2) in each experiment. It must be kept in mind that the eigenfunctions can all be multiplied by an arbitrary complex number, because if $\phi_n(x_i)$ is an eigenfunction, so is $\exp(ia)\phi_n(x_i)$ where a is an arbitrary constant. In other words, the vectors (complex numbers) defining an eigenfunction can all be rotated by an arbitrary angle. We have arbitrarily chosen the first element of the eigenvector to have a zero phase angle.

TABLE 6. Some experiments with complex empirical eigenfunction decomposition.

| Experi-ment	Stations involved	First mode				Second mode			
		ϕ_1	λ_1 (cm² s⁻²)	Per-cent	$\langle E_1^*(0+i\tau_w)\rangle$	ϕ_2	λ_2 (cm² s⁻²)	Per-cent	$\langle E_2^*(0+i\tau_w)\rangle$
1	NH3, 30 m	0.59 exp(i0°)				0.69 exp(i0°)			
	NH10, 40 m	0.61 exp(−i14°)	485.3	78.5	0.56 exp(−i0.2°)	0.32 exp(−i142°)	91.6	14.8	0.25 exp(i18.4°)
	NH15, 40 m	0.39 exp(−i24°)				0.31 exp(i150°)			
	NH20, 40 m	0.40 exp(−i14°)				0.58 exp(i126°)			
	Aster, 20 m	0.43 exp(i0°)				0.58 exp(i0°)			
	Aster, 40 m	0.33 exp(i4°)				0.23 exp(i7°)			
2	Carnation, 20 m	0.32 exp(−i3°)				0.69 exp(i170°)			
	Carnation, 40 m	0.38 exp(i5°)				0.30 exp(−i178°)			
	Carnation, 60 m	0.43 exp(i3°)	728.9	81.1	0.59 exp(i1.2°)	0.08 exp(−i176°)	75.2	8.4	0.22 exp(−i4.0°)
	Carnation, 80 m	0.39 exp(i5°)				0.05 exp(−i48°)			
	Carnation, 95 m	0.31 exp(i6°)				0.03 exp(−i7°)			
	Forsythia, 40 m	0.11 exp(i9°)				0.14 exp(−i45°)			
	Forsythia, 80 m	0.09 exp(−i9°)				0.08 exp(−i26°)			
	Forsythia, 120 m	0.08 exp(−i4°)				0.06 exp(−i63°)			
	Forsythia, 180 m	0.08 exp(−i7°)				0.03 exp(−i103°)			
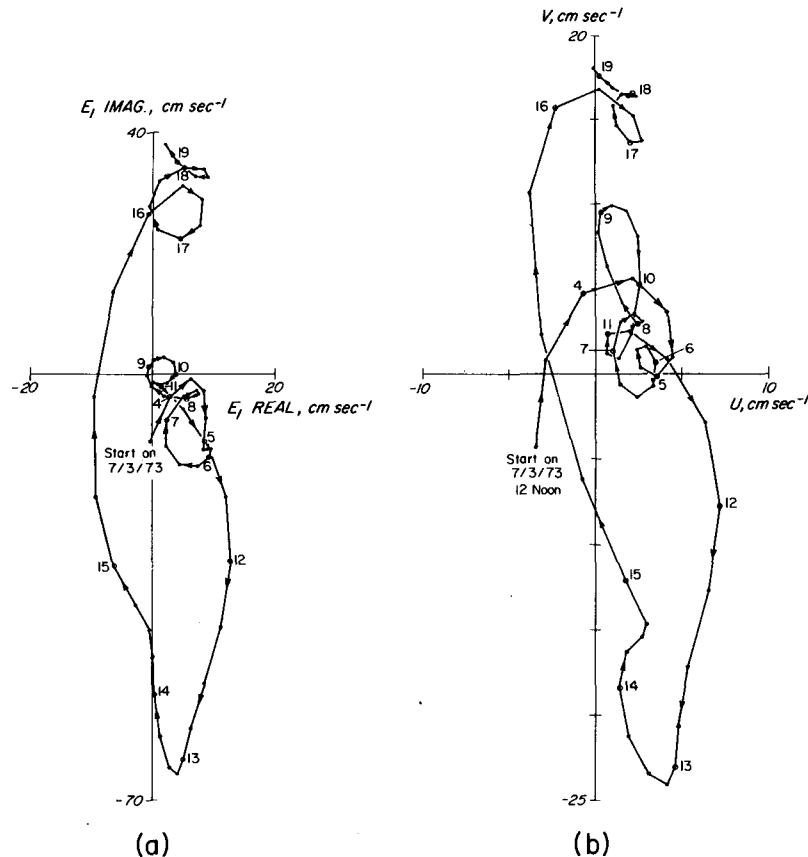
FIG. 12. Hodograph plots of (a) E_1 in Experiment 2 and (b) the 80 m current at *Carnation*. In both (a) and (b), only the early part of the total time series has been drawn for clarity. The zero hour on each day has been indicated by open circles and labeled. Six-hourly values have been indicated by dots.

In Experiment 1 in Table 6, we find the complex empirical eigenfunctions on an east-west line at 40 m depth during CUE-1. The shape of the first eigenfunction shows the counterclockwise rotation of the current fluctuations as one goes offshore, a manifestation of the "topographic steering" mentioned in Section 4.

Experiment 2 in Table 6 is the decomposition on a two-dimensional east-west cross section. The shape of the first mode, which accounts for 81% of the variance, shows that the simultaneous current fluctuations are roughly in the same direction and decrease offshore. A hodograph plot of $E_1(t)$ is shown in Fig. 12a. Since this mode accounts for such a high fraction of the energy, the hodograph may be interpreted as a vector representation of most of the currents on the shelf. For comparison, the hodograph of the 80 m current at *Carnation* is shown in Fig. 12b. The consistent clockwise rotation in both of these plots is in agreement with the behavior expected of continental shelf waves.

The plot of $E_1(t)$ in Fig. 12 shows in particular the strong response of the current over the shelf to the wind event of 11–16 July (Kundu *et al.*, 1975; Halpern, 1975). At the beginning of this event the alongshore component

of the wind, which was weak and toward the north during 6–9 July, changes direction and blows toward the south. It increases in magnitude from 11 July to a maximum (low-pass filtered) value of 11 m s^{-1} on 13 July, after which it decreases. The response of the currents on the shelf as represented by $E_1(t)$ is characterized by an increase in magnitude southward and onshore, which is in qualitative agreement with the expected behavior during an upwelling-favorable wind event. The overall behavior of the currents from 11–16 July describes a large clockwise ellipse in the hodograph.

Note that there are also some smaller clockwise ellipses in Fig. 12 (e.g., 16–18 July) with period of about 2 days. An examination of the wind data (Fig. 3 of Kundu *et al.*, 1975) shows that these current fluctuations were generally not accompanied by corresponding alongshore wind fluctuations. The coherence between the currents and the wind was also found to be low at these frequencies (Kundu *et al.*, 1975). It therefore seems that these relatively weak current fluctuations could be due to free continental shelf waves. The dispersion diagram in Cutchin and Smith (1973) indicates that at these relatively short periods it is only possible

to have free waves belonging to the first mode, which propagate at about 250 km day^{-1}. These weaker fluctuations do not, however, greatly affect the correlation calculations of Section 6, which showed that the energetic signals in 1973 propagates at about 120 km day^{-1}.

9. Nearshore behavior

Theoretical results from idealized, inviscid, time-dependent models for the response of stratified coastal regions to meteorological forcing [summarized as they might apply here, e.g., by Kundu et al. (1975) and Allen (1976)] indicate that the largest amplitude baroclinic motion should occur in a region close to the coast with an offshore scale of the order of the Rossby radius of deformation δ_R. Off the Oregon coast in this region, during the upwelling season, we find $\delta_R \approx 16$ km (Kundu et al., 1975). Since this is a fundamental implication of idealized, theoretical upwelling models, it is important to ask to what extent the measurements confirm this result. It has been mentioned in previous studies (e.g., Smith, 1974; Kundu et al., 1975), that the hydrographic data show the major motion of density surfaces in the upwelling regime off Oregon, outside of the surface layer and on time scales of several days, to be within 10 km of the coast, thus supporting qualitatively the theoretical result. Here the low-frequency current fluctuations near the coast are examined in light of the theoretical prediction.

In Kundu et al. (1975) the behavior of the barotropic and baroclinic components of the currents at DB7 during 1972 and at Carnation during 1973 was studied. Both of these stations were at a distance of ~13 km from the coast, i.e., they were within the theoretical estimate for δ_R, but they were seaward of the region (<10 km) where the relatively large motion of density surfaces was observed. It was possible in that study to offer an explanation, based on results from the idealized theoretical model, for the time-dependent behavior and relation to the wind stress, of the barotropic part of the alongshore current v. The time-dependent behavior of the baroclinic component of v, however, was not as easy to understand and no satisfactory explanation was achieved. To investigate further the baroclinic behavior, we make here a corresponding examination of the current measurements at a station which is closer to the coast than either DB7 or Carnation. Specifically, we examine the currents at Aster, which was inshore of Carnation on the same onshore-offshore line, and was approximately 5 km from the coast, i.e., well within both δ_R and the region of observed large-amplitude motion of the density field.

Since, in general, the behavior of the alongshore component of the current v appears to be easier to understand than that of u, probably because of superposition of "turbulence," we concentrate on the v component at Aster and on its relation with the wind stress and with the currents at Carnation.

TABLE 7. Some properties of the dynamic and empirical modes at Aster and Carnation.

1. Structure of dynamic mode at Aster:

	Z_1	Z_2
20 m	1.0	0.63
40 m	1.0	−0.38

2. Mean and SD:

		Mean (cm s^{-1})	SD (cm s^{-1})
Aster	D_{1v}	− 4.9	10.3
	D_{2v}	−10.3	5.8
Carnation	D_{1v}	−15.1	9.9
	D_{2v}	−20.7	5.8

3. Correlation coefficients at Aster:

$\langle D_{1v}E_{1v}\rangle = 0.99$ $\langle D_{2v}E_{2v}\rangle = 0.82$
$\langle D_{1v}\tau_w\rangle = 0.58$ $\langle D_{2v}\tau_w\rangle = 0.06$

4. Correlation coefficients between Aster and Carnation:

$\langle D_{1v_A}D_{1v_C}\rangle = 0.82$ $\langle D_{2v_A}D_{2v_C}\rangle = -0.07$

We note that at Aster the structure of ϕ_{1v}, the first empirical orthogonal function for v (Table 3), contains some vertical shear, with the larger value of ϕ_{1v} near the surface. Since the first mode carries a very large percent (95%) of the energy, this implies that the major part of the motion of the fluctuating v components at Aster involves a vertical shear. In addition, the magnitude of the shear increases in absolute value as the amplitude of the mode increases in absolute value. This is in contrast to the behavior at Carnation where the fluctuating v components are much more nearly depth-independent and consequently so is ϕ_{1v}. This type of behavior is also present in the 1972 measurements along the NH line, where there is a vertical shear in ϕ_{1v} at NH6 and a more nearly depth-independent structure at NH10 and NH20. There is, however, considerable shear in ϕ_{1v} at NH15 also, which spoils the simple picture. The reason is not clear, but it may be due to the fact that NH15 is directly north of Stonewell Bank (see, e.g., Huyer et al., 1974), by about 15 km which may well affect the motion at NH15, where a northward mean flow was observed near the bottom.

To investigate further the question of baroclinic motion at Aster, the v components were decomposed into dynamic modes in the same manner as used for the currents at Carnation and DB7 in Kundu et al. (1975). A smoothed average density structure was calculated from eight profiles of σ_t taken near Aster during the upwelling season (Holbrook and Halpern, 1974). The continuous structures of the barotropic mode Z_1 and the first barclinic mode Z_2 are not shown, but their values at 20 and 40 m are given in Table 7. The velocity components were decomposed such that

$$v(z_i,t) = D_{1v}(t)Z_1(z_i) + D_{2v}(t)Z_2(z_i). \qquad (9.1)$$

The mean values and standard deviations of D_{1v} and D_{2v} for both *Aster* and *Carnation* are given in Table 7. It may be seen that the standard deviations of D_{2v} are of a similar magnitude for *Aster* and *Carnation*, as are the standard deviations of D_{1v}. There is no evidence on this basis, therefore, that the magnitude of the baroclinic fluctuations represented by D_{2v}SD increase, either in absolute magnitude or relative to D_{1v}SD, on going inshore from *Carnation* to *Aster*.

It is interesting to compare the modal structure of the empirical orthogonal functions and the dynamic modes. As mentioned, ϕ_{1v} includes a vertical shear, whereas Z_1 is depth-independent. If ϕ_{1v} is written as a combination of Z_1 and Z_2, $\phi_{1v} = aZ_1 + bZ_2$, we obtain $a/b = (0.67/0.22) = 3.12$ which indicates that Z_1 is the major component of ϕ_{1v}. In fact, in spite of the structural differences between ϕ_{1v} and Z_1, we find an extremely high value for the correlation coefficient between D_{1v} and E_{1v} and a high value for that between D_{2v} and E_{2v} (Table 7).

If we examine the correlation between the barotropic and baroclinic components at *Aster* and the corresponding components at *Carnation*, we find that the D_{1v}'s are highly correlated, but that the D_{2v}'s are essentially uncorrelated (Table 7). The same trend is indicated by the values of the corresponding E_{1v}'s and E_{2v}'s (Table 4). Evidently, the baroclinic component at *Aster* is not strongly related to that at *Carnation*. We also find (Table 7) that D_{1v} at *Aster* has about the same correlation with the wind stress τ_w as does E_{1v}, and that D_{2v} is essentially uncorrelated with τ_w.

With the exception of the vertical shear that appears in ϕ_{1v} at *Aster* and at NH6, there is little direct support for the predictions of the previously mentioned theoretical models from the above results concerning the velocity fluctuations. A reason may be provided by the distortion of the basic state. The density field within δ_R of the coast varies substantially during the upwelling season in response to the events caused by strong upwelling-favorable winds (Smith, 1974; Kundu et al., 1975; Halpern, 1975). Also, since δ_R is a relatively small scale of the same order as that of alongshore variations in the bottom topography, it might be expected that appreciable alongshore variations in the basic density field develop within δ_R. These factors, along with the presence of a mean current, may cause the basic state of the density field to be too complex to be modeled properly with the approximations of the idealized theories.

10. Summary

Two distinct types of coastal jets have been found in this region, a mean jet which is baroclinic and a fluctuating jet which is largely barotropic. The mean jet $\bar{v}$, which has a considerable vertical shear with the surface currents flowing southward relative to the bottom currents, has a maximum speed near the surface at a distance of approximately 15–20 km from the coast, inshore of which it appears to approach zero at the coastal boundary. The fluctuating part of the alongshore velocity, on the other hand, has the structure of a roughly barotropic jet, where the maximum value seems to be obtained very close to the shore, in a distance less than 5 km from the coast. (This behavior is similar to that in a turbulent boundary layer where the mean velocity feels retarding effects much further away from the wall than is felt by the fluctuations themselves.) This is not unexpected, since the mean speed is retarded through frictional effects generated by the Reynolds stresses of the fluctuations, which are large where the fluctuations are large, whereas the fluctuations themselves are retarded due to still smaller scale motions. A mechanism for the production of a steady-state baroclinic coastal jet was found theoretically by Allen (1973) in a two-dimensional model and was based on the effects of upwelling and diffusion. The same mechanism is also operative in three-dimensional models (Pedlosky, 1974a,b). The fluctuating barotropic jet may be produced by free continental shelf wave modes, which may be superimposed and used in the description of forced motion (Gill and Schuman, 1974).

There does not appear to be a great deal of direct support in these velocity measurements for the results of idealized, stratified, inviscid flat bottom models of the coastal response problem. These models predict a large baroclinic response within a distance of the order of the Rossby radius of deformation δ_R ($\sim$15 km) from the coast. Although the density field seems to respond with the largest fluctuations within δ_R, the fluctuating alongshore velocity field does not show a large baroclinic component which behaves in obvious accordance with the qualitive features of the theory. This may be due to the presense of distortions of the density field near the coast, both in time and in alongshore direction, which are large enough that the idealized basic state of the theoretical models is not an adequate approximation. The fluctuating velocity does, however, seem to have an increased vertical shear at the inshore stations, but the depth-independent mode is still the major component.

The onshore-offshore fluctuations u, which are of the same order as the alongshore fluctuations at a large ($\sim$40 km) distance from the coast, appear to decrease as the coastal boundary is approached. The u components also show a smaller correlation length than is shown by the v components, presumably because the wave-induced u's, which are smaller than the wave induced v's, get submerged in the background "turbulence."

A scatter diagram of the velocity fluctuations at different stations demonstrates that the fluctuations are clearly topographically steered. The sign of the Reynolds stresses in this region, therefore, is controlled mainly by the bathymetry. A continuous trace of these

scatter plots also revealed the consistent clockwise rotation of the current fluctuations in the hodograph plane, adding more support to the suggestion that the major portion of the current fluctuations is composed of (forced or free) continental shelf waves.

Since the energetic components are of major interest, the alongshore propagation speed of these wave motions was found from the time lag corresponding to maximum correlation between alongshore stations. The fluctuations in the alongshore velocity were found to propagate northward approximately nondispersively in the range $0 < \omega < 0.4$ cpd at a mean speed of 500 km day^{-1} during 1972 and at 120 km day^{-1} during 1973.

REFERENCES

Allen, J. S., 1973: Upwelling and coastal jets in a continuously stratified ocean. *J. Phys. Oceanogr.*, **3**, 245–257.
——, 1976: Some aspects of the forced wave response of stratified coastal regions. *J. Phys. Oceanogr.*, **6**, 113–119.
Buchwald, V. T., and J. K. Adams, 1968: The propagation of continental shelf waves. *Proc. Roy. Soc. London*, **A305**, 235–250.
Comte-Bellot, G., 1965: Écoulement turbulent entre deux parois parallèles. *Publ. Sci. Tech. Ministère de l'air*, No. 419.
Cutchin, D. L., and R. L. Smith, 1973: Continental shelf waves: Low-frequency variations in sea level and currents over the Oregon continental shelf. *J. Phys. Oceanogr.*, **3**, 73–82.
Gill, A. E., and E. H. Schumann, 1974: The generation of long shelf waves by wind. *J. Phys. Oceanogr.*, **4**, 83–90.
Halpern, D. 1975. Structure of a coastal upwelling event observed off Oregon during July 1973. *Deep Sea Res.* (in press).
——, and J. R. Holbrook, 1972: STD measurements off the Oregon coast during July/August 1972. CUEA Data Report No. 4.
Holbrook, J. R., and D. Halpern, 1974: STD measurements off the Oregon coast during July/August 1973. CUEA Data Report No. 12.
Huyer, A., R. L. Smith and R. D. Pillsbury, 1974: Observations in a coastal upwelling region during a period of variable winds (Oregon coast, July 1972). *Tethys*, **6**, 391–404.
——, B. M. Hickey, J. D. Smith, R. L. Smith and R. D. Pillsbury, 1975: Alongshore coherence at low frequencies in currents observed over the continental shelf off Oregon and Washington. *J. Geophys. Res.*, **80**, 3495–3505.
Kundu, P. K., 1976: A note on the Ekman veering observed near the ocean bottom. *J. Phys. Oceanogr.*, **6**, 238–242.
——, J. S. Allen and R. L. Smith, 1975: Modal decomposition of the velocity field near the Oregon coast. *J. Phys. Oceanogr.*, **5**, 683–704.
Lumley, J. L., and H. A. Panofsky, 1964: *The Structure of Atmospheric Turbulence.* Wiley, 239 pp.
Mooers, C. N. K., and R. L. Smith, 1968: Continental shelf waves off Oregon. *J. Geophys. Res.*, **73**, 549–557.
Pedlosky, J., 1974a: On coastal jets and upwelling in bounded basins. *J. Phys. Oceanogr.*, **4**, 3–18.
——, 1974b: Longshore currents, upwelling and bottom topography. *J. Phys. Oceanogr.*, **4**, 214–226.
Phillips, O. M., 1969: *The Dynamics of the Upper Ocean.* Cambridge University Press, 261 pp.
Pillsbury, R. D., J. S. Bottero, R. E. Still and W. E. Gilbert, 1974: A compilations of observations from moored current meters, Vols. VI and VII. Refs. 74–2 and 74–7, School of Oceanography, Oregon State University.
Smith, R. L., 1974: A description of current, wind, and sea level variations during coastal upwelling off the Oregon coast, July/August 1972. *J. Geophys. Res.*, **79**, 435–443.
Townsend, A. A., 1956: *The Structure of Turbulent Shear Flow.* Cambridge University Press, 315 pp.